Simulation of Bifacial and Monofacial Silicon Solar Cell Short-Circuit Current Density Under Measured Spectro-Angular Solar Irradiance

Shweta Pal, Angèle Reinders, and Rebecca Saive

***Abstract*—In this article, we simulated the performance of bifacial and monofacial silicon heterojunction solar cells under measured spectro-angular solar irradiance. We developed a new set-up and procedure to measure spectro-angular irradiance over a wide range of orientations. Measurements were executed in Enschede, the Netherlands (52°23′ N, 6°85′ E). Using this measured multi-dimensional input irradiance along with SunSolve simulated external quantum efficiency for various cells, we determined the short-circuit current density of bifacial and monofacial silicon heterojunction solar cells. We conclude that monofacial cells perform marginally better than bifacial cells for front-side illumination (up to 3.0% more for direct sun) and bifacial cells perform significantly better than monofacial cells (higher output ranging from 20.1% to 68.1%), under diffuse irradiance. We compared our results with a well-monitored roof-top solar module set-up and found good agreement for clear sky days (accuracy 1.1%–8.5%).**

***Index Terms*—Bifacial cells, diffuse irradiance, PV performance, silicon solar cells, solar spectra, spectral and angular irradiance, spectro-angular irradiance.**

I. Introduction

THE output of a silicon solar cell, amongst other factors, depends on the following:

1) the spectral irradiance [1], [2];
2) the angle of incidence [3];
3) the temperature of the cell [4]; and
4) the solar cell's device design.

In several technologies, the output is particularly dependent on the spectral and angular irradiance.

1) Two-terminal tandem and multi-junction silicon solar cells are sensitive to changes in the spectrum due to current matching constraints [5], [6], which get enhanced for light that is not incident under normal angle.
2) Bifacial solar cells accept light from the front and rear side and, hence, capture a higher portion of diffuse irradiance and ground reflected irradiance (albedo), thus increasing output [7]. This has motivated research in various directions for bifacial cells, ranging from mismatch loss estimation [8], single-axis tracking [9], [10], modeling [11] to field studies [12]. Furthermore, it has been shown that the spectral dependence of albedo also strongly influences the output [13]–[15]. Properly accounting for all these effects requires knowledge on the spectral and angular irradiance.
3) Various emerging light management strategies also impart angular dependences [16]–[21], thus, emphasizing on the need to take into account the spectral and angular profile of the incoming irradiance to calculate PV performance.

Traditionally, the AM 1.5 spectrum [22] is used as the standard incoming irradiance, neglecting that in reality, irradiance depends on location [23], time of the day [24] and year [25], local climate [26] and weather [27], cloud coverage [28], and surroundings [29]. The actual incident irradiance consists of direct beam irradiance and diffuse irradiance. Diffuse irradiance results from scattering on atmospheric molecules, clouds, and small particles. In countries with cloudy climates, diffuse irradiance caused by clouds contributes significantly to the incident irradiance energy. In the Netherlands, for instance, diffuse irradiation amounted to around 55% for the year 2017 [30].

Irradiance monitoring devices like pyranometers and pyrheliometers and various other sophisticated irradiance modeling strategies [31]–[37] provide a highly reliable method to analyze PV performance. But these methods do not give information on the spectral and angular composition of the incoming irradiance. Ignoring the spectral and angular distribution of the solar irradiance can lead up to an error of 15% in the simulated PV power for a monocrystalline silicon module [38]. Even sophisticated computational simulations developed to account for as many parameters as possible, still stress on the requirement of more local and reliable input irradiance [39], [40], in order to determine PV performance more accurately, among which is the short-circuit current density.

The time and location-dependent solar irradiance in combination with the spectrum and angle-dependent performance of solar cells establishes the need to have an angle-resolved spectral irradiance map, henceforth referred to as spectro-angular irradiance. In 2016, one of first efforts in modeling the spectral and angular irradiance was presented by Ernst *et al.* [41]. Yet,

Manuscript received September 14, 2020; accepted September 17, 2020. Date of publication October 9, 2020; date of current version October 21, 2020. The work of Shweta Pal and Rebecca Saive were supported by the University of Twente tenure-track start-up funding. *(Corresponding author: Shweta Pal.)*

Shweta Pal and Rebecca Saive are with the MESA+ Institute for Nanotechnology, Inorganic Materials Science, Faculty of Science and Technology, University of Twente, 7522 NB, Enschede, The Netherlands (e-mail: s.s.pal@utwente.nl; r.saive@utwente.nl).

Angèle Reinders is with the Faculty of Engineering Technology, Department of Design, Production and Management,University of Twente, 7522 NB Enschede, The Netherlands (e-mail: a.h.m.e.reinders@utwente.nl).

Color versions of one or more of the figures in this article are available online at https://ieeexplore.ieee.org.

Digital Object Identifier 10.1109/JPHOTOV.2020.3026141

an extensive experimental validation is missing. Therefore, in this article, we explore a method to measure the spectro-angular irradiance for various sky conditions throughout the year and quantify its effect on different solar cell configurations. All the experiments described in this work were carried out in Enschede, the Netherlands (52°23′ N, 6°85′ E).

The structure of the article is as follows: Section II elaborates on the seasonal solar spectrum variation. Section III elaborates on the experimental set-up and procedure and comments on the sky conditions of the experiments. Section IV presents the computational simulation of external quantum efficiency (EQE) and the method of short-circuit current density calculation used. Subsequently, the results obtained are summarized in Section V and the article is completed by a discussion and conclusion in Section VI.

II. Seasonal Solar Spectrum Variation

To get an overview of the solar resource available across a year, we look at the seasonal variation in the spectral irradiance recorded for the year 2014. The spectral measurements were performed using a south facing spectroradiometer tilted at 30° with respect to the zenith. The spectroradiometer is an EKO MS 700, with spectral range of 350–1050 nm and accuracy of ±10.89% for 350–450 nm, ±4.13% for 450–900 nm, and ±4.06% for 900–1050 nm. This set-up is located at the PV test bench at the University of Twente, Enschede, the Netherlands [42]. To visualize the large changes in irradiance spectra throughout the year, we choose to plot the spectrum for solar noon of a given month for the day with maximum irradiance at solar noon [see Fig. 1(a)] and minimum irradiance at solar noon [see Fig. 1(b)]. The day with maximum irradiance for a given month was determined by selecting the spectrum with the highest peak value. Similarly, the day with the lowest total irradiance was determined by selecting the spectrum with the lowest peak value. We see that the spectral content changes significantly over the course of a year. As we go from winter (January) to summer (June), the irradiance increases gradually. Similarly, as we move from summer (June) to winter (December), the irradiance gradually decreases. The largest changes are seen for the lower wavelengths. Also, the peak values for days with the highest irradiance [see Fig. 1(a)] is about ten times greater than the peak value for days with the lowest irradiance [see Fig. 1(b)]. As the incoming radiation varies throughout the year, these variations must be taken into account for solar power output calculations. An analysis of this test bench data expanding on the results reported here can be found in [42] and [43]. While these continuous spectral measurements are a crucial step to the better understanding of irradiance changes and their influence on PV output, as we describe in the introduction, we still need to take into account the angle resolved irradiance instead of a constant tilt angle capturing one specific hemisphere.

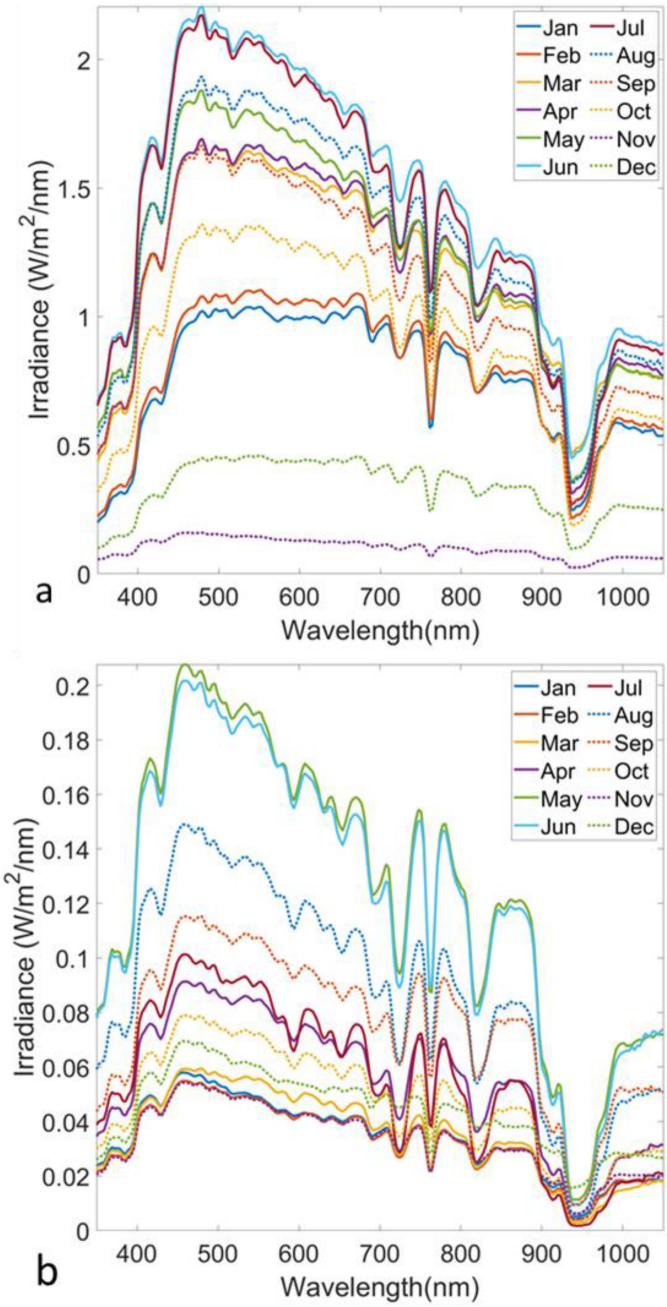

Fig. 1. Maxima of spectra measured in each month of the year 2014 for Enschede, the Netherlands. (a) For a day with maximum total irradiation. (b) For a day with minimum total irradiation.

III. Spectro-Angular Irradiance Measurements

We designed and developed a set-up and procedure to measure spectro-angular solar irradiance [30], [44]. Here, we present a thorough analysis of this spectro-angular irradiance recorded in Enschede, the Netherlands (52°23′ N, 6°85′ E). The data were recorded for various times of the day and year, and sky conditions as detailed in Table I. The set-up, data acquisition, and measurements are described in the following sections.

A. Spectro-Angular Irradiance Measurement Set-Up

The spectro-angular irradiance measurement set-up [see Fig. 2(a)] consists of a fiber-coupled spectrometer supported by

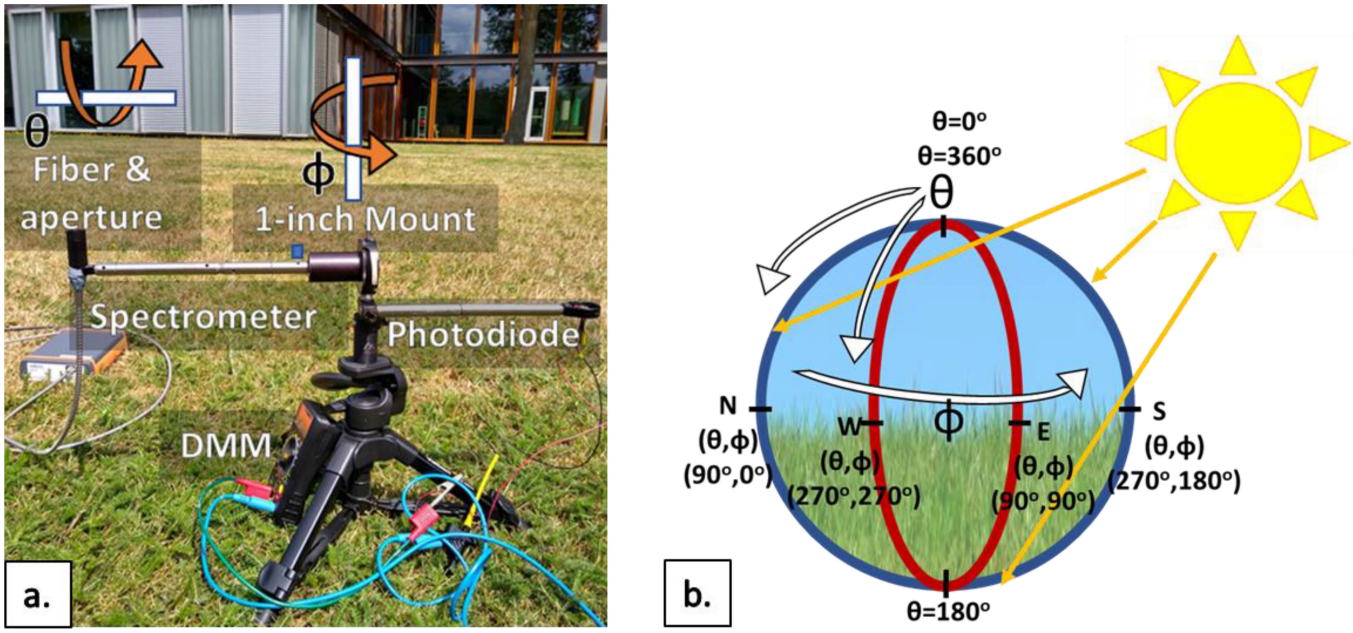

Fig. 2 (a) Photograph of the spectro-angular irradiance measurement setup. (b) Schematic demonstrating the angle definition.

TABLE I
DATE AND TIME OF THE MEASUREMENTS

Date	Sky condition	Time slot	Sun's position (θ, ϕ)
07/21/2019	Cloudy	12:28-13:48	$(32.29^{\circ}, 194.57^{\circ})$
07/23/2019	Clear	08:35-09:02	$(54.80^{\circ}, 102.86^{\circ})$
	Clear	12:14-12:43	$(32.14^{\circ}, 174.66^{\circ})$
	Clear	16:15-16:48	$(55.22^{\circ}, 257.75^{\circ})$
03/21/2020	Clear	10:17-10:59	$(58.71^{\circ}, 143.00^{\circ})$
	Cloudy	12:44-13:28	$(52.89^{\circ}, 187.59^{\circ})$
	Clear	14:55-15:26	$(61.13^{\circ}, 223.47^{\circ})$
03/25/2020	Clear	10:09-10:33	$(59.07^{\circ}, 137.23^{\circ})$
	Fairly clear	12:41:13:11	$(51.13^{\circ}, 184.96^{\circ})$
	Fairly clear	14:40-15:13	$(58.34^{\circ}, 220.88^{\circ})$

a tripod and 1 inch rotation mount. The spectrometer used was an Avantes CMOS device, with a bandwidth of 200 to 1100 nm, and accuracy of $\pm 5\%$. The rotation mount and the tripod allow the fiber to rotate along the zenith and azimuth angle axis, respectively, thus enabling the fiber to point in any direction. For controlling the viewing angle, we used an aperture with a cosine corrector attached to the fiber. For the work presented here, the viewing angle was fixed to be 23°. With a viewing angle of 23° and the need to keep the experiment duration small, the step size was decided to 30°. But often, test modules or irradiance sensors are positioned at 45° from the zenith. To ensure that we can cross-check our approach with such sensors, the step size decided was 30° and 45°, leading to 17 different measurement points in one series to cover a plane. Due to this reason, the measurement series may take 30 to 90 minutes, the cloud coverage may vary drastically within the course of the experiment. To monitor and quantify these changes, we used a photodiode which was set horizontally, facing the zenith, i.e., the sky. The viewing angle of the photodiode was approximately 140°.

B. Measurement Procedure

Three sets of measurements were performed as follows:

1) direct sun (DS);
2) north-south plane (NS); and
3) east-west plane (EW).

Throughout the entire report, we use spherical co-ordinates defined by (radius, zenith angle, azimuth angle) $= (r, \theta, \phi)$, with the radius (r) is set to unity. This is to maintain consistency with popular irradiance models [31]–[37], and measuring instruments [45]. This definition of angular orientation differs from the standard polar coordinates. The NS plane is defined as $\phi = 0^{\circ}$, or $\phi = 180^{\circ}$, and $0^{\circ} \leq \theta \leq 360^{\circ}$, where (θ, ϕ) values for north and south are $(90^{\circ}, 0^{\circ})$ and $(270^{\circ}, 180^{\circ})$, respectively [see Fig. 2(b)]. Similarly, the EW plane is defined as $\phi = 90^{\circ}$, or $\phi = 270^{\circ}$, and $0^{\circ} \leq \theta \leq 360^{\circ}$, where (θ, ϕ) values for east and west are $(90^{\circ}, 90^{\circ})$ and $(270^{\circ}, 270^{\circ})$, respectively. The NS and EW plane measurements were performed by aligning the fiber accordingly using a compass and recording data at angular steps of 30° or 15° (to account for 45°) along the θ-axis. The measurement began from zenith, i.e., 0° and ended at zenith again, i.e., 360°. The direct sun spectrum was recorded by pointing the fiber tip of the detector towards the sun and adjusting it further for maximum signal. Simultaneous to the DS, NS, and EW spectral measurements, the photodiode current was recorded.

C. Spectro-Angular Irradiance Data

The measurements were performed for two different times of the year, i.e., summer (July 21, 2019 and July 23, 2019) and spring (March 21, 2020 and March 25, 2020). We begin by analyzing the spectral measurements for some specific angles, namely,

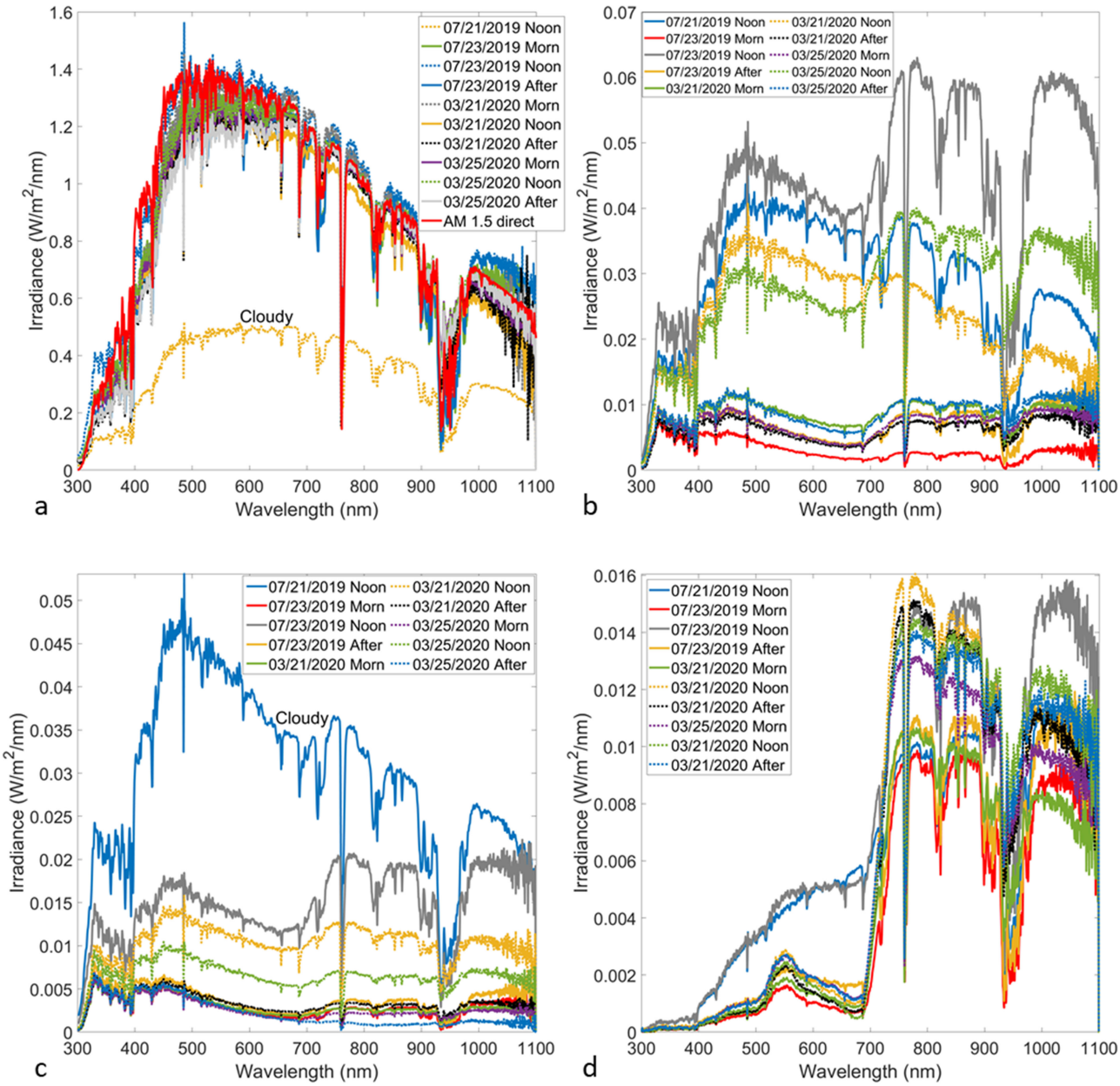

Fig. 3. Spectral plots for (a) direct sun, (b) 30° tilted South facing [$(\theta, \phi) = (330°, 270°)$], (c) zenith for NS plane [$(\theta, \phi) = (0°, 0°)$], (d) albedo for NS plane [$(\theta, \phi) = (0°, 180°)$]. For the direct sun [see Fig. 3(a)], the measurements for all days follow the same trend as AM 1.5 direct spectrum (red), except July 21, 2019 as heavy cloud coverage blocked the sun. In Fig. 3(b), for the spectral output for a 30° tilted south facing sensor, we see the noon-time has a higher output than other times of the day. Particularly, it is highest for summer noon (July 21, 2019 and July 23, 2019). In the case of the zenith angle [see Fig. 3(c)], we notice that July 21, 2019 has the highest output as the heavy cloudy diffuses incident irradiance in zenith direction. In Fig. 3(d), we see the spectral albedo plots (NS plane) showing a small bump around 550 nm indicating the presence of green grass.

1) direct sun;
2) 30° tilted South facing [$(\theta, \phi) = (330°, 270°)$];
3) zenith for NS plane [$(\theta, \phi) = (0°, 0°)$]; and
4) albedo for NS plane [$(\theta, \phi) = (0°, 180°)$].

Since the EQE of silicon heterojunction cells start to vanish beyond 1100 nm (also discussed in Section IV-B), this work focuses on the wavelength range 300–1100 nm. Therefore, all the measurement equipment used (photodiode for normalization and CMOS spectrometer for spectral measurements) were silicon-based.

Fig. 3(a) displays the spectral plots for direct sun. The measurements for all days follow the similar curve as AM 1.5 direct spectrum (red), except July 21, 2019 Noon. This was due to heavy cloudy coverage blocking the sun. Fig. 3(b) shows the spectral output for a 30° tilted south facing sensor. We see that the noon-time has a higher output than other times of the day, and the signal is highest for summer noon (July 21, 2019 Noon and July 23, 2019 Noon), as expected. Moreover, the detectors used for Fig. 1(a) and (b) and Fig. 3(b) have the same orientation, yet they have different curves. This is due to the difference

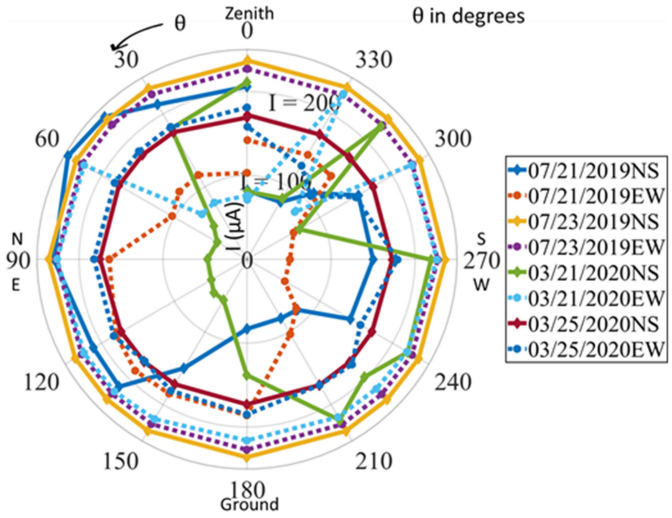

Fig. 4. Current of a horizontally positioned photodiode (I in μA) versus all the zenith angles of the fiber under noon sky for all the mentioned days. This plot indicates the variation of cloud coverage over time. Changing cloud coverage results in fluctuating current versus angle plots and this variation is used to normalize the spectro-angular irradiance measurements.

in the viewing angle of the detectors. The spectroradiometer (used for Fig. 1(a) and Fig. 1(b)) has a 180° viewing angle, which enables the detector to capture all the irradiance coming from the entire upper hemisphere, including the direct sun. And as mentioned earlier, the fiber-coupled spectrometer has a 23° viewing angle. This leads to the exclusion of direct sun irradiance in the cases when the sun's location is not within the fiber's viewing angle. In the case of the zenith angle [see Fig. 3(c)], we notice that July 21, 2019 Noon has the highest output as the heavy cloud coverage diffuses incoming irradiance in the zenith direction. This is in agreement with the conclusion that for a cloudy day, fixed horizontal orientation is the best configuration [46]. Finally, Fig. 3(d) shows the spectral plots for the ground, i.e., albedo, for NS plane. The curves have a small bump around 550 nm indicating the presence of green grass. The curves for summer noon (July 21, 2019 Noon and July 23, 2019 Noon) are different as compared to the rest of the sky conditions.

D. Irradiance Measurements

In this section, we evaluate the changes in cloud coverage during our measurements for the mentioned days. Fig. 4 shows a polar plot of the photodiode current (I in μA) versus zenith angle of the fiber for noon sky for all the mentioned days. This figure shows the variation of cloud coverage over the course of the spectro-angular measurements. For all polar plots presented in this article, the north and south are represented by 90° and 270° on the NS plane respectively, and the east and west are represented by 90° and 270° on the EW plane respectively. The current changes by a small percentage for clear sky days (e.g., 3.4% for July 21, 2019NS about the average). For the cloudy days, we see fluctuating current output indicating fluctuating cloud coverage. We use this variation in current to normalize the irradiance curves for all the spectro-angular measurements, i.e., all the measurements are referenced to the photodiode current for the direct sun. Through this procedure, we remove the effect of varying cloud coverage while recording data for one specific set of measurements.

IV. Computational Simulation and Calculations

In this section, we describe the computational simulations and calculations performed to model EQE for monofacial (Mo) and bifacial (Bi) silicon heterojunction solar cells.

A. Computational Simulations for EQE

We used SunSolve by PV Lighthouse [47], which runs ray tracing and transfer matrix-based Monte-Carlo simulations to calculate EQE. The software takes the geometry and complex refractive index data for every material as input and calculates reflection, transmission, and absorption of every layer. The EQE is assumed to be equivalent to the absorption within the active layer, i.e., the internal quantum efficiency is assumed to be one, which is a valid assumption for silicon heterojunction solar cells [48]. The EQE was simulated for 10 angles equally spaced between 0° to 89° and interpolated for any other angles in between. The EQE was set to zero for the edges of the cell (90° and 270°). The cells used in this article have the same architecture and materials as the cells used in [49]. For both types of cells, the active absorber layer consists of 180 μm thick crystalline Si [50] with top and bottom surface being textured with 5 μm high random upright pyramids. The top and bottom of the active absorber are passivated by 5 nm amorphous intrinsic Si [48]. Selective contacts of 5 nm of amorphous n-Si [48] on the top and 5 nm amorphous p-Si [48] on the bottom are assumed with 70 nm of indium tin oxide [51] on each of them. The final bottom layer for a monofacial cell is a 300 nm thick Ag [52]. The cells are encapsulated in 450 μm thick EVA [53] followed by 3.2 mm of glass [54] and finally 110 nm thick ARC [55].

Fig. 5(a) shows EQE plots for a bifacial cell for various angles starting from 0° to 180°. The EQE decreases as the angle is changed from 0° to 90° and increases in a similar fashion again between 90° and 180°. The difference in EQE of symmetric angles of the top and bottom surface resulted from the difference in parasitic absorption of p-Si on top and n-Si on the bottom. In the case of a monofacial cell, EQE for angles from 270° to 90° (front surface) is similar to that of a bifacial cell, except for the infrared region. In Fig. 5(b), a comparison between a monofacial and a bifacial cell is shown for 0°, 45°, and 90°. A monofacial cell has better performance in the infrared region because the silver rear reflector redirects infrared light back into the cell, thereby increasing the optical path length. Due to the silver mirror, absorption on the rear surface is not possible and we set the EQE for all the angles ranging from 90° to 270° to zero.

B. Short-Circuit Current Density Calculations

In order to examine the output of bifacial and monofacial cells for various tilt settings, a normal to the cell surface was defined and its orientation is given in Table II. Because of

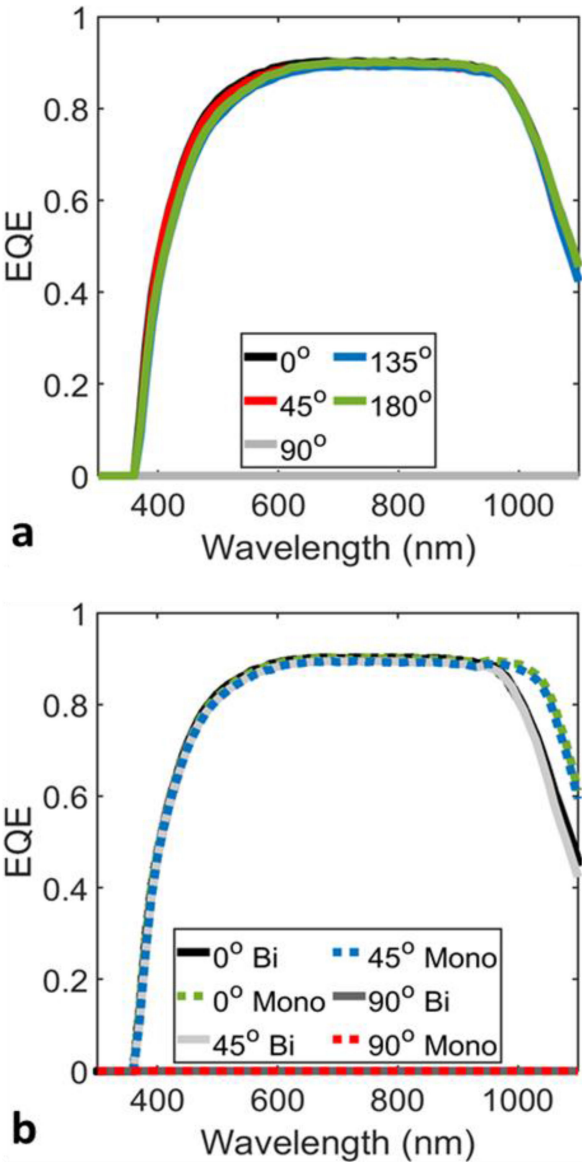

Fig. 5. EQE plots for various angles of (a) a bifacial cell and (b) a bifacial and a monofacial cells. For a bifacial cell, EQE for top and bottom hemisphere not identical due to n and p layer, respectively. For a monofacial cell, EQE in the infra-red region is higher than bifacial cell due to Ag rear reflector.

this varying tilt and the difference in the sun's position for various sky conditions, the angle (ψ) between the cell and the incoming radiation changes. Short-circuit current density ($J_{\theta,\phi}$) for a particular zenith (θ) and azimuth (ϕ) angle for a solar cell is calculated using the following equation:

$$J_{\theta,\phi} = q \int_{300}^{1100} F(\lambda,\theta,\phi) \cdot \cos(\psi) \cdot EQE(\lambda,\psi)\ d\lambda \qquad (1)$$

where F is the flux, ψ is the angle between the cell normal and the incoming radiation, and λ is the wavelength. The numerical integration was done using the trapezoidal rule.

The flux is obtained by converting the units of irradiance measurements in the experiment (see Section III) and the EQE is obtained by computational simulations (see Section IV). For convenience, the short-circuit current density will be referred to as "output" or simply "current density.".

TABLE II
ORIENTATION OF THE NORMAL OF THE MODULE FOR VARIOUS CONFIGURATIONS

Cell Configuration	Angular orientation (θ, ϕ)
Horizontal	($0^\circ, 0^\circ$)
45° South	($45^\circ, 180^\circ$)
Vertical NS	($90^\circ, 180^\circ$)
Vertical EW	($90^\circ, 90^\circ$)

The current density for each angle, for direct and diffuse irradiance, is calculated using the above equation. But in the case of diffuse irradiance, to calculate the total current density incident from all the angles and over all the wavelengths, first, we calculate the current density by each plane, i.e., J_{NS} and J_{EW} for the respective NS and EW planes, separately using the following equation:

$$J_{\mathrm{plane}} = \sum_{\theta=0^\circ}^{330^\circ} J_{\mathrm{plane},\theta} * \rho \qquad (2)$$

where ρ is the angle fraction and given as follows:

$$\rho = \frac{\text{angular step size}}{\text{viewing angle}} \qquad (3)$$

where the viewing angle is 23° and the step size either 15° or 30°. Concretely, the measured angles were 0°, 30°, 45°, 60°, 90°, 120°, 135°, 150°, 180°, 210°, 225°, 240°, 270°, 300°, 315°, 330°, 360°.

The total short-circuit current density (J_{Total}) is given as the average of J_{NS} and J_{EW} as follows:

$$J_{\mathrm{Total}} = \frac{J_{\mathrm{NS}} + J_{\mathrm{EW}}}{2}\ . \qquad (4)$$

We then compute bifacial gain (BG) in terms of short-circuit current density for direct and diffuse irradiance, as given by the following equation:

$$\mathrm{BG} = \frac{J_{\mathrm{Bi}} - J_{\mathrm{Mono}}}{J_{\mathrm{Bi}}} * 100. \qquad (5)$$

The above-mentioned diffuse irradiance calculations are done and analyzed separately for total diffuse irradiance, diffuse irradiance from the upper hemisphere (from 270° to 90°) and from the lower hemisphere (from 90° to 270°).

Generally, the performance of solar modules is described by calculating or measuring power conversion efficiencies, which require the knowledge of open-circuit voltage (V_{OC}) and fill factor (FF). Both quantities are dependent on module temperature [56], which requires knowledge of ambient temperature, wind speed, and heat dissipation of the components of the module [57]. These parameters were unavailable to us. Hence, in the work presented here, the performance of the module is discussed only in terms of short-circuit current density.

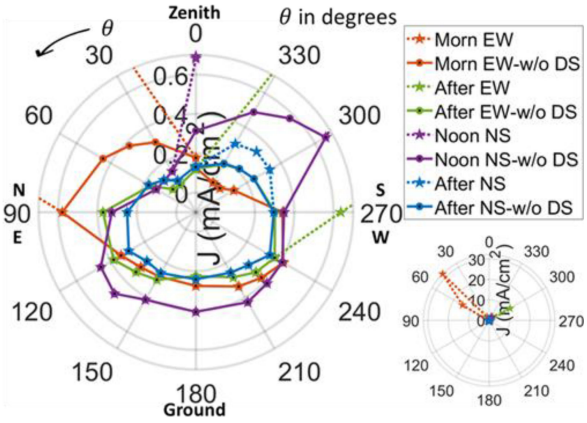

Fig. 6. Maximum current density (EQE = 1 and cosine = 1 with respect to polar angle, for certain cases for July 23, 2019. Output with the DS influence is shown with dotted lines and output after eliminating DS, i.e., only diffuse irradiance, is shown with solid line. Inset: Zoomed out polar plot of maximum current density for all the sky conditions.

V. Results

In summary, we calculated the short-circuit current density for monofacial and bifacial heterojunction silicon cells, by combining the measured multidimensional input irradiance (see Section III) with computationally simulated EQE (see Section IV) according to (1). For the input irradiance, the direct and diffused component was separated first. Then the calculations were performed for various sky conditions (as mentioned previously) and various cell tilt and orientation (detailed in Table II). These cell configurations are denoted as follows:

1) horizontal cell (Horizontal);
2) cell tilted at 45° with respect to zenith facing south (45° South); and
3) vertical cell facing north-south (Vertical NS), d) vertical cell facing east-west (Vertical EW).

In the following sections, we discuss some results obtained for direct and diffuse irradiance.

A. Separation of Direct and Diffuse Irradiance Component

Fig. 6 displays a polar plot of the maximum short-circuit current density (in mA/cm^2) possible for certain cases for July 23, 2019. This equivalent maximum current density is calculated by setting EQE to 1 (indicating perfect absorption and perfect internal quantum efficiency across the whole spectrum) and the cosine term to be 1 (indicating normal incidence) in (1). For angles closer to the sun's location, the direct sun was within the chosen aperture and therefore, falsified the measured irradiance, as seen by dotted lines in the figure. To correct for this, we take out the measurements for these angles and linearly interpolate. The results of this interpolation for certain sky conditions for July 23, 2019 can be seen with solid curves in the same figure.

B. Polar Plot of Current Density Under Diffuse Irradiance

Fig. 7(a)–(h) shows polar plots of the current density for various cell configurations with only diffuse irradiance for noon sky of July 21, 2019 (cloudy sky), and July 23, 2019 (clear sky), including maximum possible output (yellow curve). The maximum possible current density assumes perfect EQE and normal irradiance for (1), which is also shown in Fig. 5. For each sky condition, a polar plot for a bifacial and a monofacial cell for NS and EW plane is shown. The current density (J) is plotted along the radial axis and has an uncertainty of $\pm 5.2\%$. Below the legend, a schematic representation of the cell orientation is given with the orange arrow representing the normal of the cell. For the maximum output curve (yellow), we see that the contribution from the bottom hemisphere is higher for the clear sky day, and for cloudy sky, the contribution from the upper hemisphere is higher.

The output for a horizontal cell (black curve) becomes zero at 90° and 270° as the EQE and the cosine becomes zero at these angles in all the figures. For the 45° south-facing cell (blue curve), the output becomes zero at 45° and 225° for NS [see Fig. 7(a), (c), (e), and (g)] and 90° and 270° for EW [see Fig. 7(b), (d), (f), and (h)] because the 45° NS and 225° NS are the 90° and 270° for such a tilted cell. In the case of vertical NS (red curve) and vertical EW (green curve) configuration [see Fig. 7(a)–(d), the 0° and 180° become the points where EQE and cosine terms become zero, hence, contributing to zero current density. Again, in Fig. 7(a), (c), (e), and (g), for vertical EW(green curve), the contribution of the irradiance coming from NS plane is zero as these light rays are parallel to the cell. Similarly, the contribution of irradiance from the EW plane to the output of vertical NS (red curve) cell is zero as the light coming from this plane travels parallel to the cell (see Fig. 7(b), (d), (f) and (h)].

On comparing the output of a bifacial cell to that of a monofacial cell, it can be seen that for any orientation, the front face of monofacial cell produces marginally higher output than its bifacial counterpart due to higher EQE in the infrared region, see also Fig. 5. A monofacial cell shows similar behavior as a bifacial cell only for one half of the circle, as only the front face is active. Due to the higher acceptance angle, a bifacial cell can accept light from almost all angles, hence accepts more diffuse irradiance and albedo. The measurements were performed on grass, the effect would be even more pronounced for a higher albedo [13]–[15]. On the other hand, if the cells were mounted on a low albedo material such as dark concrete, the benefit of a bifacial cell would only result from improved performance during cloudy days. We would like to note that in a large power plant with several modules next to each other, self-shading would also become relevant and our measurements and calculations would have to be adjusted accordingly. Another interesting case is a bifacial cell in vertical EW configuration (green curve) which is one of the best settings for morning and afternoon sky, since it has better performance for the east and west direction, as shown by the two lobes in Fig. 7(b) and (f). Thus, for a cloudy sky setting and/or high albedo surrounding, bifacial cell clearly becomes a better-suited candidate. Also, during the sunrise and sunset hours, the power consumption increases [58], and thus, an increase in power production during these hours can help bridge the gap between consumption and production.

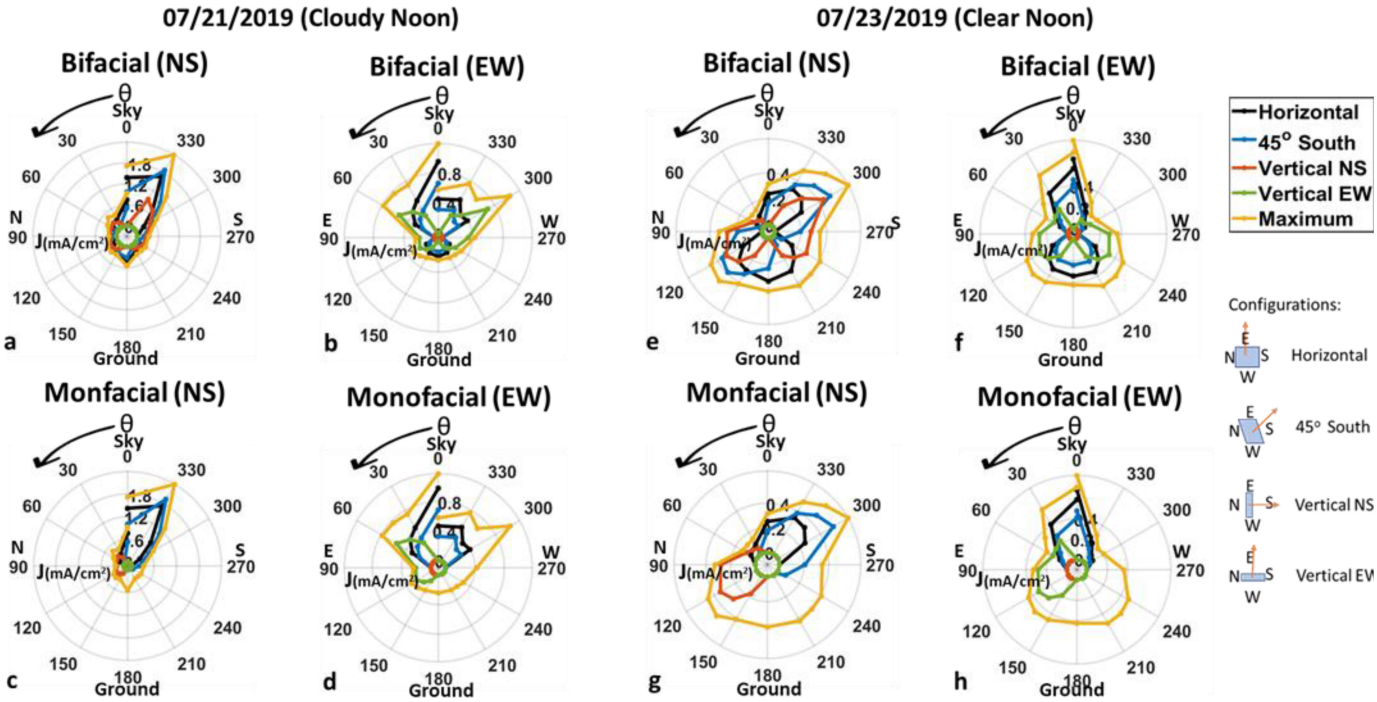

Fig. 7 (a)–(h) Polar plot of current densities for bifacial and monofacial cells under noon sky for July 23, 2019 (cloudy sky) and July 21, 2019 (clear sky) condition (diffuse) for all configurations. (a), (c), (e), and (g) correspond to calculations done with radiation measured in the NS plane and (b), (d), (f), and (h) correspond to calculations done with radiation measured in the EW plane. The yellow curve shows the maximum possible output, i.e., EQE = 1 and cosine = 1 in (1). In the case of July 23, 2019 (clear sky), we notice that the contribution of the bottom hemisphere is more than the upper hemisphere, and for July 21, 2019 (cloudy sky), the upper hemisphere contributes the most. We see that a monofacial cell produces a similar curve to that of a bifacial cell but only for one half, i.e., the active side. For vertical EW configuration (green curve) (a), (c), (e), (g), the contribution by NS plane is zero, and vice versa is true for vertical NS configuration (red curve) [in 7(b), (d), (f), (h)]. Here, we get a detailed account of angle-resolved current density for a given cell in various configurations.

C. Total Current Density (J_{Total})

To obtain an overall picture of the performance of bifacial and monofacial solar cells under various illumination conditions and cell configurations, a comparison of their total outputs, i.e., total current density (J_{Total}), is required. This total current density output is calculated by using (1) and (4) and the results are graphically presented in Fig. 8(a)–(c). Fig. 8(a) shows the results for direct irradiance and Fig. 8(b) and (d) for total diffuse irradiance (entire 360°), upper diffuse irradiance (from 270° to 90°), and the lower diffuse irradiance (from 90° to 270°), respectively.

The bars show the maximum possible output [i.e., cosine is 1 and EQE is 1 for (1)] of each day for the direct irradiance [see Fig. 8(a)], total diffuse irradiance [see Fig. 8(b)], diffuse irradiance on the upper hemisphere [see Fig. 8(c)] and the lower hemisphere [see Fig. 8(d)]. The white and red markers indicate the output of bifacial and monofacial cells, respectively. Different orientations of the cells are shown by different shapes of markers.

The maximum output (bars) for the direct sun [see Fig. 8(a)] is the highest for clear noon skies, except for the noon of March 21, 2020. This is due to the fact that there was considerable cloud coverage, as indicated by Fig. 4. As expected, the maximum output for the direct sun is lowest for cloudy (July 21, 2019) noon sky. Also, the total diffuse maximum output [in Fig. 8(b)] for July 21, 2019 noon and March 21, 2020 noon sky is considerably higher than other days due to cloudy sky. As the cloud coverage increases, the diffused fraction increases and the direct irradiance decreases.

To compare the performance of bifacial and monofacial cells, we first look at their output for each type of irradiance. In the case of direct irradiance beam only [see Fig. 8(a)], a bifacial cell practically behaves like a monofacial cell as the irradiance falls on only one face at a time. We notice that because of the higher infrared EQE, a monofacial cell has a higher output than a bifacial cell for every case, except for vertical EW configuration under clear noon sky for which both cells have almost no output. For noon sky and afternoon sky, the total current density by a monofacial cell in vertical EW setting is zero, due to the direct sunbeam being at the back (non-active) side of the monofacial cell (refer to sun's position in Table I). In crux, the best output for morning and afternoon sky is seen with vertical EW configuration with a monofacial and a bifacial cell, respectively—however, only if the active side of the monofacial cell is facing east, as it was the case here. For noon sky, 45° south configuration is optimum, as the difference between the normal of the cell and the sun is the least.

Fig. 8(b)–(d) shows a comparison of performance under diffuse irradiance. For the full hemisphere diffuse irradiance [see Fig. 8(b)], a bifacial cell performs better in any configuration for any sky condition, with horizontal orientation being the best, followed by 45° south configuration. To have a better

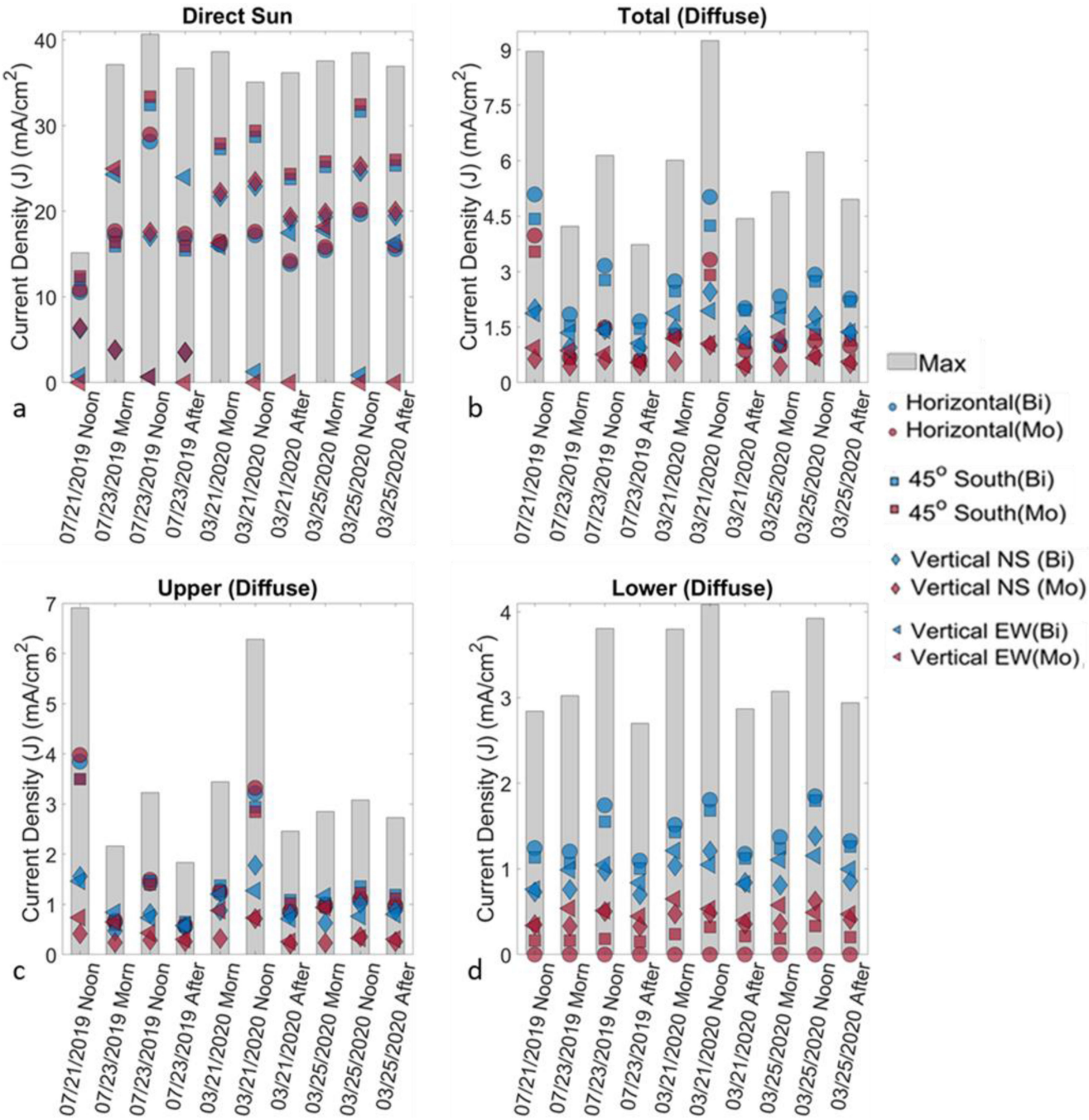

Fig. 8. Total current densities for bifacial and monofacial modules for all investigated sky conditions and configurations under (a) direct irradiance, (b) total diffuse irradiance, (c) upper diffuse irradiance, and (d) lower diffuse irradiance. Monofacial cells give zero output for direct sun when the sun is on the non-active side, as expected. For direct sun and upper diffuse radiation, a monofacial cell performs better. But for lower diffuse irradiance, a bifacial cell has far superior performance, which consequently leads to a higher total diffuse irradiance output.

understanding of output contribution coming from various directions, we look into the output due to diffuse irradiance coming from the upper hemisphere (majorly owing to clouds and atmosphere) and the lower hemisphere (majorly albedo). Fig. 8(c) shows a comparison of diffuse irradiance from the upper hemisphere. Again, for the upper hemisphere, a monofacial cell produces more because it has a higher EQE in the infra-red region for the side which faces the upper hemisphere. For the lower hemisphere (light gray bar), the output of a monofacial cell for horizontal configuration is zero as expected due to the non-active side. Also, a bifacial cell performs significantly better than a monofacial cell as it is capable of absorbing the irradiance from the bottom. The contribution by the lower hemisphere, i.e., albedo, is so significant that the output under the total diffuse irradiance by a bifacial cell becomes higher than a monofacial cell. In a nutshell, due to better EQE for the infrared region, a monofacial cell has a marginally higher output than a bifacial cell, when only one face of a bifacial is active, e.g., under direct

		07/21/2019	07/23/2019			03/21/2020			03/25/2020		
		Noon	Morn	Noon	After	Morn	Noon	After	Morn	Noon	After
Horizontal	Direct	-3.0	-2.8	-3.0	-3.0	-2.3	-2.4	-2.4	-2.4	-2.6	-2.7
	Total (Diffuse)	21.9	63.3	52.8	64.2	53.4	33.8	56.6	57.2	61.6	56.5
	Upper (Diffuse)	-3.4	-5.4	-5.1	-5.8	-4.3	-3.3	-4.3	-4.2	-4.4	-4.2
	Lower (Diffuse)	100.0	100.0	100.0	100.0	100.0	100.0	100.0	100.0	100.0	100.0
45° South	Direct	-3.0	-2.8	-3.0	-3.0	-2.4	-2.4	-2.5	-2.4	-2.6	-2.7
	Total (Diffuse)	20.1	58.4	47.8	58.1	46.9	31.5	45.4	50.8	52.6	47.4
	Upper (Diffuse)	0.0	10.8	4.5	12.2	8.1	3.1	5.7	7.2	9.2	6.5
	Lower (Diffuse)	85.5	84.5	88.3	84.8	83.2	80.9	81.0	85.0	81.5	83.9
Vertical NS	Direct	-3.0	-1.6	-3.0	-1.7	-2.3	-2.4	-2.5	-2.4	-2.6	-2.7
	Total (Diffuse)	68.1	53.3	57.9	52.6	60.4	58.8	66.6	59.9	59.3	62.7
	Upper (Diffuse)	73.5	49.0	65.0	51.4	63.5	59.6	73.6	63.6	64.8	70.3
	Lower (Diffuse)	52.1	56.2	48.4	52.8	54.2	60.2	57.8	54.9	54.8	52.4
Vertical EW	Direct	100.0	-2.8	7.7	100.0	-2.3	100.0	100.0	-2.4	100.0	100.0
	Total (Diffuse)	49.7	35.7	46.5	49.1	36.3	45.8	59.2	31.0	55.9	58.9
	Upper (Diffuse)	49.6	22.9	41.3	47.7	27.1	42.5	63.8	19.3	57.1	62.0
	Lower (Diffuse)	55.5	45.4	51.0	46.7	46.5	49.2	51.6	47.9	57.4	52.7

Fig. 9. Bifacial short-circuit current density gain calculated using (5) for various sky conditions and configurations for direct, total (diffuse), upper (diffuse), and lower (diffuse) irradiance. Each module has a horizontal histogram depicting the gain by each configuration and condition. Red bars indicate that a monofacial cell produces more current than a bifacial one, and green indicates higher current generation by bifacial modules. Due to better EQE in the infrared region, a monofacial module performs better mainly in the cases of direct sun (when sun is on the active side) and upper (diffuse) illumination. Bifacial modules perform better in every other case because of a higher acceptance angle, thus capturing more light.

sun and diffuse irradiance from the upper hemisphere. But when the whole viewing angle of a bifacial cell and the contribution of albedo is considered, the output of a bifacial cell surpasses that of a monofacial cell significantly. This can be clearly seen for the cases of diffuse irradiance from the lower hemisphere and ultimately, the total diffuse irradiance. Thus, when the albedo is further improved, it can lead to even higher power generation by a bifacial cell. Another advantage that a bifacial cell offers is the freedom to choose the best configuration. A bifacial cell, in all cases, gives nearly an output as high as that of a monofacial cell. But in certain special cases, like vertical EW configuration, it produces significantly higher output, as it can absorb irradiance during the morning and the evening from either of the faces.

D. Bifacial Short-Circuit Current Density Gain

Fig. 9 shows bifacial short-circuit current density gain calculated using (5), for various sky conditions and configurations for direct, total (diffuse), upper (diffuse), lower (diffuse). Each cell has a horizontal bar depicting the gain by that particular cell configuration and sky condition. Red bars indicate that a monofacial cell produces more output than a bifacial cell, up to 3.0% for direct sun and up to 5.9% for upper (diffuse) illumination. Due to better EQE in the infrared region, a monofacial cell performs better mainly in the cases of direct sun (when the sun is on the active side) and upper (diffuse) illumination. Green bars indicate higher output generation by bifacial cell, ranging from 20.1% to 68.1% for total (diffuse) irradiance. The gain can be as high as 100% for horizontally oriented cell, if only lower (diffuse) hemisphere illumination is considered. A bifacial cell performs better for every other case because of higher acceptance angles, thus capturing more incident irradiance.

E. Validation of the Computational Method

To test our calculations involving spectro-angular irradiance, we computed current densities for a realistic outdoor solar module under various sky conditions and compared our results to the output of a test bench solar module. The module under observation was a south-facing monofacial multicrystalline silicon solar panel (Canadian Solar CS6P-245P), tilted at 30° from the zenith. The module is located at the PV test bench at the University of Twente, Enschede, the Netherlands with a 400 m distance to where the spectro-angular measurements were taken. The set-up logs a current value (in Amperes) every minute.

For a given sky condition, we selected module current values corresponding to exact instances of each angular measurement and then converted them into current density (mA/cm^2). These values were then averaged.

For the calculations, we simulated EQE for the module and combined it with the spectro-angular irradiance measurements to obtain total current density, using (1)–(4). Since we were dealing with an outdoor module, we wanted to ensure that we were normalizing the flux (using photodiode current) with the exact same sky condition that the module was exposed to. For this, we ran the calculations for various iterations, where each iteration corresponded to normalization with respect to the photodiode current for one particular angle. This leads to 34 total current density values as there were 34 angles in total (17 for NS and EW plane, each). These 34 values were then averaged to obtain a final calculated total current density for the module and the standard deviation is reported as error bar in Fig. 10(a).

The results for the above-mentioned computation are shown in Fig. 10(a). We notice that the measured and the calculated output is the highest for the July 23, 2019 Noon, as expected. The

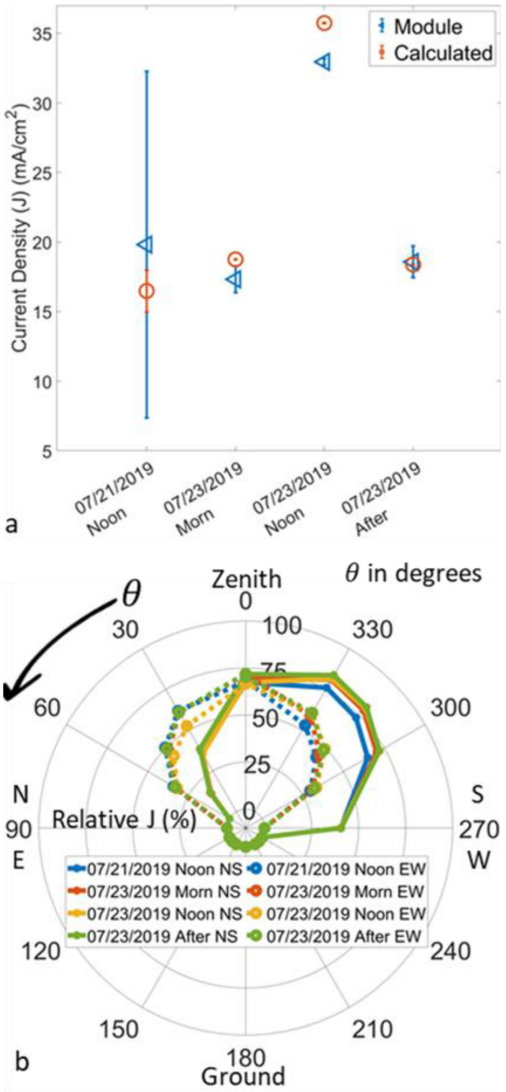

Fig. 10. (a) Plot of averaged measured and calculated current density for the module under various sky conditions. The calculated and the measured values match well. We see higher-relative error for July 21, 2019 due to cloudy and fluctuating sky condition and smaller relative error for 07/23/2019 due to clear sky condition. (b) Polar plot of the relative current density (in %) for the module under various diffuse sky conditions compared to the maximum possible current density. We see zero current density generation at the non-active side of the monofacial module. This can be improved by using a bifacial cell and optimizing the tilt and height of the module, and albedo accordingly.

calculated and measured values for July 23, 2019 morning and afternoon are similar because the sun's position was symmetric to solar noon (refer Table I). Overall, for July 23, 2019, the sky was clear and stable (refer Fig. 4), hence, the standard deviation is lower. For July 21, 2019 Noon, the measured and calculated output is low as the sky was cloudy and fluctuating (refer Fig. 4). As a consequence, the standard deviation for July 21, 2019 is large ($\pm 62.9\%$) for module measurements. The standard deviation for the calculated value is significantly smaller ($\pm 9.1\%$). This is because, while collecting the spectro-angular data, the signal was low, thus, leading to higher integration time (often longer than a minute). This resulted in an overall time-averaged spectral data for that given angle, consequently, reducing the standard deviation of the final calculated value. To quantify the agreement between the measurements and calculation, per cent accuracy was defined as follows:

$$\text{Per cent accuracy } = \left(\frac{|X_{\text{calc}} - X_{\text{exp}}|}{X_{\text{exp}}}\right) * 100 \qquad (6)$$

where X_{calc} is the calculated value, X_{exp} is the expected value, i.e., measured value of the module (provided $X_{\text{exp}} \neq 0$), and the modulus sign ($|\ |$) represents absolute value.

From the obtained values of percent accuracy, we can conclude that the current densities we calculated from our spectro-angular irradiance measurements are in very good agreement with measured test bench solar cell data for clear sky day (July 23, 2019), ranging from $\pm 1.1\%$ to $\pm 8.5\%$. For cloudy sky (July 21, 2019), this value turns out to be $\pm 16.8\%$, which can be improved by making a few upgrades to the set-up described in Section III-A. First, the set-up can be automated to reduced measurement time so as to minimize cloud coverage variation within the measurement window. This will enable one to gather irradiance data over long term, thus, improving reliability. Second, the photodiode that is used for normalization can be replaced with another calibrated spectrometer that constantly faces the zenith to monitor the sky. This is because the photodiode does not give information about the instantaneous spectral variation due to fluctuating cloud coverage. A spectrometer will address this issue.

In order to obtain angle-resolved information of the output generation of the module, a polar plot of fractional calculated current density under diffuse irradiance is shown in Fig. 10(b). For a given angle, the fractional current density is the ratio of the current density of the module to the maximum possible current density (i.e., perfect EQE and normal incidence). This gives a better idea of how much energy is unused or lost for a given direction/angle. Again, we notice that the edges of the module produce zero output at 60° and 240° for the NS plane (solid lines), and at 0° and 180° (dotted lines) for the EW plane. The irradiance on the non-active side of the module is completely unused. This can be improved by replacing the monofacial module with a bifacial one. Moreover, optimizing the tilt angle and the height of the module, and the albedo will further increase output.

We would like to note that the presented study did not consider the mounting height and self-shading, rather, the presented data can be fed into more complete algorithms, replacing simulated or simplified irradiance by real, location-specific spectro-angular irradiance data. Cell temperature was not considered either as it cannot be derived directly from irradiance without knowledge on ambient temperature, humidity, and wind speed.

VI. Discussion and Conclusion

We have presented a novel method to simulate the current density output of solar cells using multi-dimensional (spectral and angular) irradiance input. A 360° spectro-angular irradiance map was measured for various times of day and year, and cloud coverage. Using this measured irradiance and computationally simulated angle-dependent EQE, short-circuit current density of monofacial and bifacial silicon heterojunction PV cells was

simulated. Through this approach, we obtained wavelength and angle-dependent performance characteristics of both types of solar cells punted in different configurations. We confirmed that monofacial cells perform marginally better than bifacial cells for front-side illumination due to increased infrared light trapping. This improvement ranges up to 3.02% for direct sun irradiance at a current density of 17.4 mA/cm^2 and up to 5.9% for upper (diffuse) irradiance at a current density of 0.6 mA/cm^2 under a clear summer afternoon sky (July 23, 2019 after), for a horizontally fixed module. We also confirmed previous studies showing that bifacial cells perform significantly better (ranging from 20.1% to 68.1%) when diffuse irradiance is incident. Using this spectro-angular data, we also computed current density for a solar module and compared it to the measured values of an outdoor solar module set-up at a well-monitored PV test bench. The computational results correspond well with the clear sky measurements (percent accuracy ranging within $\pm$1.1%–$\pm$8.5%), thus validating the method for stable clear sky. This serves as motivation to extend this approach to obtain detailed knowledge on power generation by solar modules even with cloudy sky, if certain modifications are made. Namely, automation for faster measurements account for instantaneous cloud-coverage variations and for data collection over a long term. Also, using spectrometer instead of a photodiode for flux normalization could help to account for spectral changes due to changing cloud coverage. Furthermore, if V_{OC} and FF can be calculated and combined with the J_{SC} calculations mentioned above, one can obtain more relevant quantities like power conversion efficiencies.

In general, the incident irradiance can be a complicated function of angle and wavelength, and dependent on the specific time and location, cloud coverage, and surroundings (mainly albedo), which heavily influences the solar cell output. Moreover, introduction of novel light management structures may also introduce spectral and angular dependences. In principle, spectro-angular irradiance measurements can allow for significantly improved accuracy of modeling, prediction, and also customization of solar cell plants. As prominent examples, investors are often interested in maximum annual yield while utility companies value electricity most during peak demand times—which imposes optimization constraints different from the first example. Furthermore, assessing the added value of high-efficiency multi-junction solar cells should carefully consider spectro-angular irradiance for accurate economic decision making. Our outlook on spectro-angular irradiance is that if such continuous and long-term multi-dimensional irradiance measurements are performed at sites which already monitor total irradiance, eventually it might become possible to extrapolate spectro-angular irradiance from the knowledge of angle-independent data.

References

[1] R. Gottschalg, T. Betts, D. Infield, and M. J. Kearney, "The effect of spectral variations on the performance parameters of single and double junction amorphous silicon solar cells," *Sol. Energy Mater. Sol. Cells*, vol. 85, no. 3, pp. 415–428, 2005.

[2] P. Faine, S. R. Kurtz, C. Riordan, and J. M. Olson, "The influence of spectral solar irradiance variations on the performance of selected single-junction and multijunction solar cells," *Sol. Cells*, vol. 31, no. 3, pp. 259–278, 1991.

[3] J. Balenzategui and F. Chenlo, "Measurement and analysis of angular response of bare and encapsulated silicon solar cells," *Sol. Energy Mater. Sol. Cells*, vol. 86, no. 1, pp. 53–83, 2005.

[4] P. Singh and N. Ravindra, "Temperature dependence of solar cell performance–An analysis," *Sol. Energy Mater. Sol. Cells*, vol. 101, pp. 36–45, 2012.

[5] F. T. Si, O. Isabella, and M. Zeman, "Too Many Junctions? A Case Study of Multijunction Thin-Film Silicon Solar Cells," *Adv. Sustain. Syst.*, vol. 1, no. 10, 2017, Art. no. 1700077.

[6] K. Araki and M. Yamaguchi, "Influences of spectrum change to 3-junction concentrator cells," *Sol. Energy Mater. Sol. Cells*, vol. 75, nos. 3/4, pp. 707–714, 2003.

[7] L. Kreinin, N. Bordin, A. Karsenty, A. Drori, and N. Eisenberg, "Experimental analysis of the increases in energy generation of bifacial over mono-facial PV modules," in *Proc. 26th Eur. Photovolt. Sol. Energy Conf.*, 2010, pp. 3140–3143.

[8] C. Deline, S. Pelaez, S. MacAlpine, and C. Olalla, "Estimating and parameterizing mismatch power loss in bifacial photovoltaic systems," *Prog. Photovolt. Res. Appl.*, vol. 28, pp. 691–703, 2020.

[9] S. A. Pelaez, C. Deline, P. Greenberg, J. S. Stein, and R. K. Kostuk, "Model and validation of single-axis tracking with bifacial PV," *IEEE J. Photovolt.*, vol. 9, no. 3, pp. 715–721, May 2019.

[10] A. C. J. Russell, C. E. Valdivia, M. R. Lewis, J. E. Haysom, and K. Hinzer, "Modelling bifacial solar energy yield for single-axis tracked systems with racking," in *Proc. Int. Conf. Numerical Simul. Optoelectron. Devices*, Ottawa, ON, Canada, 2019, pp. 61–62.

[11] M. T. Patel *et al.*, "Temperature dependent energy gain of bifacial PV farms: A global perspective," 2020, *arXiv:2003.03660*.

[12] J. Stein, D. Riley, M. Lave, C. Hansen, C. Deline, and F. Toor, "Outdoor field performance from bifacial photovoltaic modules and systems," in *Proc. 44th IEEE Photovolt. Spec. Conf.*, Washington, DC, 2017, pp. 3184–3189.

[13] T. C. R. Russell, R. Saive, and H. A. Atwater, "Thermodynamic efficiency limit of bifacial solar cells for various spectral albedos," in *Proc. 44th IEEE Photovolt. Spec. Conf.*, Washington, DC, 2017, pp. 1531–1536.

[14] T. C. R. Russell, R. Saive, A. Augusto, S. G. Bowden, and H. A. Atwater, "The influence of spectral albedo on bifacial solar cells: A theoretical and experimental study," *IEEE J. Photovolt.*, vol. 7, no. 6, pp. 1611–1618, Nov. 2017.

[15] M. Brennan, A. Abramase, R. Andrews, and J. Pearce, "Effects of spectral albedo on solar photovoltaic devices," *Sol. Energy Mater. Sol. Cells*, vol. 124, pp. 111–116, 2014.

[16] I. Haedrich *et al.*, "How cell textures impact angular cell-to-module ratios and the annual yield of crystalline solar modules," *Sol. Energy Mater. Sol. Cells*, vol. 183, pp. 181–192, 2018.

[17] R. Saive, T. C. R. Russell, and H. A. Atwater, "Enhancing the power output of bifacial solar modules by applying effectively transparent contacts (ETCs) with light trapping," *IEEE J. Photovolt.*, vol. 8, no. 5, pp. 1183–1189, Sep. 2018.

[18] J. M. Delgado-Sanchez and I. Lillo-Bravo, "Angular dependence of photonic crystal coupled to photovoltaic solar cell," *Appl. Sci.*, vol. 10, no. 5, 2020, Art. no. 1574.

[19] J. M. Luque-Raigón, J. Halme, and C. López-López, "Angular optical behavior of photonic-crystal-based dye-sensitized solar cells," *J. Photon. Energy*, vol. 9, no. 2, 2019, Art. no. 025501.

[20] D. Chen *et al.*, "Nanophotonic light management for perovskite–silicon tandem solar cells," *J. Photon. Energy*, vol. 8, no. 2, 2018, Art. no. 022601.

[21] L. Einhaus and R. Saive, "Free-space concentration of diffused light for photovoltaics," in *Proc. 47th IEEE Photovolt. Spec. Conf.*, 2020.

[22] Standard tables for terrestrial direct normal solar spectral irradiance for air mass 1.5, ASTM E891-87, 1987.

[23] E. G. Laue, "The measurement of solar spectral irradiance at different terrestrial elevations," *Sol. Energy*, vol. 13, no. 1, pp. 43–50, 1970.

[24] S. Wang, "Pavement albedo assessment: Methods, aspects, and implication," Master's thesis, Iowa State Univ., Ames, IA, USA, 2015.

[25] SOLMET hourly solar radiation-surface meteorological observations – Final Report, Nat, Climatic Center, Asheville, NC, USA, 1979.

[26] E. F. Fernández, F. Almonacid, J. Ruiz-Arias, and A. Soria-Moya, "Analysis of the spectral variations on the performance of high concentrator photovoltaic modules operating under different real climate conditions," *Sol. Energy Mater. Sol. Cells*, vol. 127, pp. 179–187, 2014.

[27] S. Ghazi and K. Ip, "The effect of weather conditions on the efficiency of PV panels in the southeast of UK," *Renewable Energy*, vol. 69, pp. 50–59, 2014.

[28] G. Pfister, R. L. McKenzie, J. B. Liley, A. Thomas, B. W. Forgan, and C. N. Long, "Cloud coverage based on all-sky imaging and its impact on surface solar irradiance," *J. Appl. Meteorol.*, vol. 42, no. 10, pp. 1421–1434, 2003.

[29] X. Yang and Y. Li, "The impact of building density and building height heterogeneity on average urban albedo and street surface temperature," *Building Environ.*, vol. 90, pp. 146–156, 2015.

[30] S. Pal and R. Saive, "Experimental study of the spectral and angular solar irradiance," in *Proc. IEEE 46th Photovolt. Spec. Conf.*, Chicago, IL, USA, 2019, pp. 3182–3186.

[31] C. A. Gueymard, "Direct solar transmittance and irradiance predictions with broadband models. Part I: Detailed theoretical performance," *Sol. Energy*, vol. 74, no. 5, pp. 355–379, 2003.

[32] C. A. Gueymard, D. Myers, and K. Emery, "Proposed reference irradiance spectra for solar energy systems testing," *Sol. Energy*, vol. 73, no. 6, pp. 443–467, 2002.

[33] C. A. Gueymard, "Clear-sky irradiance predictions for solar resource mapping and large-scale applications: Improved validation methodology and detailed performance analysis of 18 broadband radiative models," *Sol. Energy*, vol. 86, no. 8, pp. 2145–2169, 2012.

[34] C. A. Gueymard, "Parameterized transmittance model for direct beam and circumsolar spectral irradiance," *Sol. Energy*, vol. 71, no. 5, pp. 325–346, 2001.

[35] J. F. Orgill and K. G. T. Hollands, "Correlation equation for hourly diffuse radiation on a horizontal surface," *Sol. Energy*, vol. 19, no. 4, pp. 357–359, 1977.

[36] R. R. Perez, J. T. Scott, and R. Stewart, "An anisotropic model for diffuse radiation incident on slopes of different orientations and possible applications to CPC's," *Proc. Annu. Meet., Amer. Sect. Int. Sol. Energy Soc.*, vol. 6, 1983.

[37] R. Perez, R. Seals, P. Ineichen, R. Stewart, and D. Menicucci, "A new simplified version of the perez diffuse irradiance model for tilted surfaces," *Sol. Energy*, vol. 39, no. 3, pp. 221–231, 1987.

[38] N. Lindsaya, Q. Libois, J. Badosa, A. Migan-Dubois, and V. Bourdin, "Errors in PV power modelling due to the lack of spectral and angular details of solar irradiance inputs," *Sol. Energy*, vol. 197, pp. 266–278, 2020.

[39] X. Sun, M. R. Khan, C. Deline, and M. A. Alam, "Optimization and performance of bifacial solar modules: A global perspective," *Appl. Energy*, vol. 212, pp. 1601–1610, 2018.

[40] S. Guo, T. M. Walsh, and M. Peters, "Vertically mounted bifacial photovoltaic modules: A global analysis," *Energy*, vol. 61, pp. 447–454, 2013.

[41] M. Ernst, H. Holst, M. Winter, and P. P. Altermatt, "SunCalculator: A program to calculate the angular and spectral distribution of direct and diffuse solar radiation," *Sol. Energy Mater. Sol. Cells*, vol. 157, pp. 913–922, 2016.

[42] L. Mutiara, K. Pegels, and A. Reinders, "Evaluation of spectrally distributed irradiance in The Netherlands regarding the energy performance of various PV technologies," in *Proc. IEEE 42nd Photovolt. Spec. Conf.*, New Orleans, LA, 2015, 2015, pp. 1–6.

[43] L. Mutiara, "Data analysis and modeling of PV performance and spectrally distributed irradiance," Univ. Twente, Enschede, The Netherlands, 2015.

[44] S. Pal and R. Saive, "Experimental study of the spectral and angular solar irradiance," in *Proc. OSA Adv. Photon. Congr.*, 2019, Art. no. PW2C.4.

[45] Kipp & Zonen. 2020. [Online]. Available: https://www.kippzonen.com/Product/11/CMP3-Pyranometer#.XyP7sCgzY-U

[46] K. A. Nelson and T. L. Gibson, "Improved photovoltaic energy output for cloudy conditions with a solar tracking system," *Sol. Energy*, vol. 83, no. 11, pp. 2092–2102, 2009.

[47] PV LightHouse, SunSolve. 2020. [Online]. Available: https://www.pvlighthouse.com.au/

[48] Z. C. Holman *et al.*, "Current losses at the front of silicon heterojunction solar cells," *IEEE J. Photovolt.*, vol. 2, no. 1, pp. 7–15, 2012.

[49] R. Saive, T. C. R. Russel, and H. A. Atwater, "Light trapping in bifacial solar modules using effectively transparent contacts (ETCs)," in *Proc. IEEE 7th World Conf. Photovolt. Energy Convers.*, Waikoloa Village, HI, 2018, pp. 0045–0048.

[50] M. A. Green, "Self-consistent optical parameters of intrinsic silicon at 300K including temperature coefficients," *Sol. Energy Mater. Sol. Cells*, vol. 92, pp. 1305–1310, 2008.

[51] Z. C. Holman *et al.*, "Infrared light management in high-efficiency silicon heterojunction and rear-passivated solar cells," *J. Appl. Phys.*, vol. 113, no. 1, 2013, Art. no. 013107.

[52] Y. Jiang, S. Pillai, and M. A. Green, "Realistic silver optical constants for plasmonics," *Sci. Rep.*, vol. 6, 2016, Art. no. 30605.

[53] M. R. Vogt *et al.*, "Optical Constants of UV Transparent EVA and the impact on the pv module output power under realistic irradiation," *Energy Procedia*, vol. 92, pp. 523–530, 2016.

[54] M. R. Vogt, H. Hahn, H. Holst, M. Winter, C. Schinke, and M. Kontges, "Measurement of the optical constants of soda-lime glasses in dependence of iron content and modeling of iron-related power losses in crystalline si solar cell modules," *IEEE J. Photovolt.*, vol. 6, no. 1, pp. 111–118, Jan. 2016.

[55] M. R. Vogt, "Development of physical models for the simulation of optical properties of solar cell modules," Ph.D. dissertation, Technische Informationsbibliothek, Hannover, Germany, 2015.

[56] M. A. Green, "General temperature dependence of solar cell performance and implications for device modelling," *Prog. Photovolt., Res. Appl.*, vol. 11, pp. 333–340, 2003.

[57] F. Lasnier, *Photvoltaics Engineering Hand-book*, Bristol, U.K.: Adam Hilger, 1990.

[58] C. Louton, J. Goodin, D. Hou, and J. Pinjuv, "Renewables Reporting," California ISO, Folsom, CA, USA, 2015.